QUANTUM SIMULATION

Realization of one-dimensional anyons with arbitrary statistical phase

Joyce Kwan[1], Perrin Segura[1], Yanfei Li[1], Sooshin Kim[1]†, Alexey V. Gorshkov[2], André Eckardt[3], Brice Bakkali-Hassani[1]‡, Markus Greiner[1]*

Low-dimensional quantum systems can host anyons, particles with exchange statistics that are neither bosonic nor fermionic. However, the physics of anyons in one dimension remains largely unexplored. In this work, we realize Abelian anyons in one dimension with arbitrary exchange statistics using ultracold atoms in an optical lattice, where we engineer the statistical phase through a density-dependent Peierls phase. We explore the dynamical behavior of two anyons undergoing quantum walks and observe the anyonic Hanbury Brown–Twiss effect as well as the formation of bound states without on-site interactions. Once interactions are introduced, we observe spatially asymmetric transport in contrast to the symmetric dynamics of bosons and fermions. Our work forms the foundation for exploring the many-body behavior of one-dimensional anyons.

In three dimensions, quantum theory admits two types of particles—bosons and fermions—depending on whether the many-body wave function acquires a phase θ of 0 (bosons) or of π (fermions) when two identical particles exchange positions. In practice, bosons prefer to occupy the same quantum state, manifested by degenerate atoms in a Bose-Einstein condensate or photons in a laser, whereas fermions obey the Pauli exclusion principle, which, for example, forces electrons to occupy different orbitals to produce elements in the periodic table. When dimensions are reduced to two, the space formed by the relative position of two identical particles is not simply connected such that exchange paths with different windings are topologically distinct, allowing the exchange phase θ to interpolate between the bosonic and fermionic limits and giving rise to fractional statistics (*1*–*3*). Particles with such nonstandard exchange phase θ are called anyons because they can acquire any phase (Fig. 1A) (*2*).

In two dimensions, where fractional statistics are typically considered, anyons arise as quasiparticle excitations in topologically ordered states of matter, such as fractional quantum Hall states (*4*–*7*) and two-dimensional (2D) spin liquids (*8*–*10*), and have gained immense interest as a key building block in fault-tolerant quantum computation (*11*–*15*). In one dimension, anyons have been defined in the context of spinon excitations in a Heisenberg antiferromagnetic chain, which were shown to obey a generalized Pauli exclusion principle allowing for fractional occupation of a quantum state (*16*). Important differences exist between 1D and 2D anyons. Whereas in two dimensions, the sign of the phase acquired by the wave function under interchange is determined by the direction of the winding, the assignment of a nontrivial phase has been shown to be possible in 1D spin chains when the crossings of the spinons are always unidirectional in accordance with their group velocities (*17*). Physically, the statistical phase manifests as a fractional shift in the linear momenta of the two particles upon crossing (*17*)—behavior that is reminiscent of the fractional shift in the relative angular momentum of 2D anyons upon exchanging positions through winding (*2*, *18*). However, 1D anyons are not associated with an intrinsic topological order, unlike their 2D counterparts.

Models of 1D systems with fractional statistics have been proposed in the continuum (*19*–*22*) and on a discrete lattice (*23*, *24*). In this work, we focus on the strongly correlated anyon-Hubbard model (AHM) (*23*), in which different paths for particle exchange may be distinguished owing to the discrete configuration space of the lattice, with the corresponding exchange phase manifesting as a Berry phase acquired around a loop in Fock space. This lattice model is predicted to host a wealth of exotic phenomena, including asymmetric momentum distributions (*23*, *25*–*27*), the continuous build-up of Friedel oscillations with increasing θ (*28*, *29*), a Mott insulator to superfluid phase transition induced by the statistical parameter θ (*23*), and a two-component superfluid phase (*30*, *31*). Recently, a topological gauge theory developed to describe 1D anyons in the continuum was realized in a weakly interacting Bose-Einstein condensate (*32*, *33*), and 1D anyonic exchange statistics have been observed in integrated photonic systems (*34*, *35*) and electric circuit simulators (*36*).

In this work, we realize 1D Abelian anyons with arbitrary statistical phase using ultracold ^{87}Rb atoms in an optical lattice. We leverage the precision and control of a quantum gas microscope (*37*) to imprint the statistical phase in a deterministic way and explore dynamical behavior through two-particle quantum walks (*38*, *39*). The system is governed by the AHM, which we realize by engineering an equivalent model, the Bose-Hubbard model (BHM) with density-dependent phase (*40*–*42*)

$$\mathcal{H} = -J\sum_j \left(b_j^\dagger e^{-in_j\theta} b_{j-1} + \text{h.c.}\right) + \frac{U}{2}\sum_j n_j(n_j-1) \quad (1)$$

where $b_j^\dagger (b_j)$ is the bosonic creation (annihilation) operator, $n_j = b_j^\dagger b_j$ is the particle number operator, J is the tunneling amplitude between neighboring sites, U is the on-site pairwise repulsive interaction energy, and $-n_j\theta$ is the density-dependent Peierls phase acquired upon tunneling to the right from site $j-1$ to site j. Note that the density-dependent phase acquired upon tunneling to the left, encapsulated in the Hermitian conjugate, is $n_j\theta$; hence, this model breaks spatial inversion symmetry, a property associated with fractional statistics (*43*). The BHM with density-dependent phase can be mapped to the AHM by a generalized Jordan-Wigner transformation (*23*, *44*).

We can gain intuition for anyons in 1D lattices by recognizing similarities with their 2D counterparts. Anyons in one dimension can be considered as bosons that create a gauge potential in the form of the density-dependent Peierls phase for other particles, analogous to the charge-flux tube composites that exemplify anyons in the 2D theory (*3*). As a result, two particles can traverse through states forming a closed loop in Fock space and acquire a phase θ corresponding to a geometric phase (Fig. 1B). This process offers an analogy to braiding in two dimensions, where tunneling right (or left) through an occupied site, which exchanges positions between particles and acquires phase −θ (or θ), corresponds to clockwise (or counterclockwise) exchange.

Engineering the AHM

We realize the BHM with density-dependent phase through Floquet engineering by modulating a tilted lattice with three frequency (three-tone) components to induce occupation-dependent tunneling processes (Fig. 1C) (*45*). Specifically, a magnetic field gradient produces an energy offset E between lattice sites to suppress tunneling, and then tunneling is reintroduced by modulating the lattice depth with three frequencies, each with amplitude δV: (i) E to tunnel from a singly occupied site to an empty site, (ii) $E + U_0$ to tunnel from a singly occupied site to a singly occupied site, and (iii) $E - U_0$ to tunnel from a doubly

[1]Department of Physics, Harvard University, Cambridge, MA, USA. [2]Joint Quantum Institute and Joint Center for Quantum Information and Computer Science, NIST/University of Maryland, College Park, MD, USA. [3]Institut für Theoretische Physik, Technische Universität Berlin, Berlin, Germany.
*Corresponding author. Email: mgreiner@g.harvard.edu
†Present address: Basic Science Research Institute, Pohang University of Science and Technology, Pohang, Gyeongbuk, Korea.
‡Present address: Laboratoire Kastler Brossel, Collège de France, CNRS, ENS-Université PSL, Sorbonne Université, Paris, France.

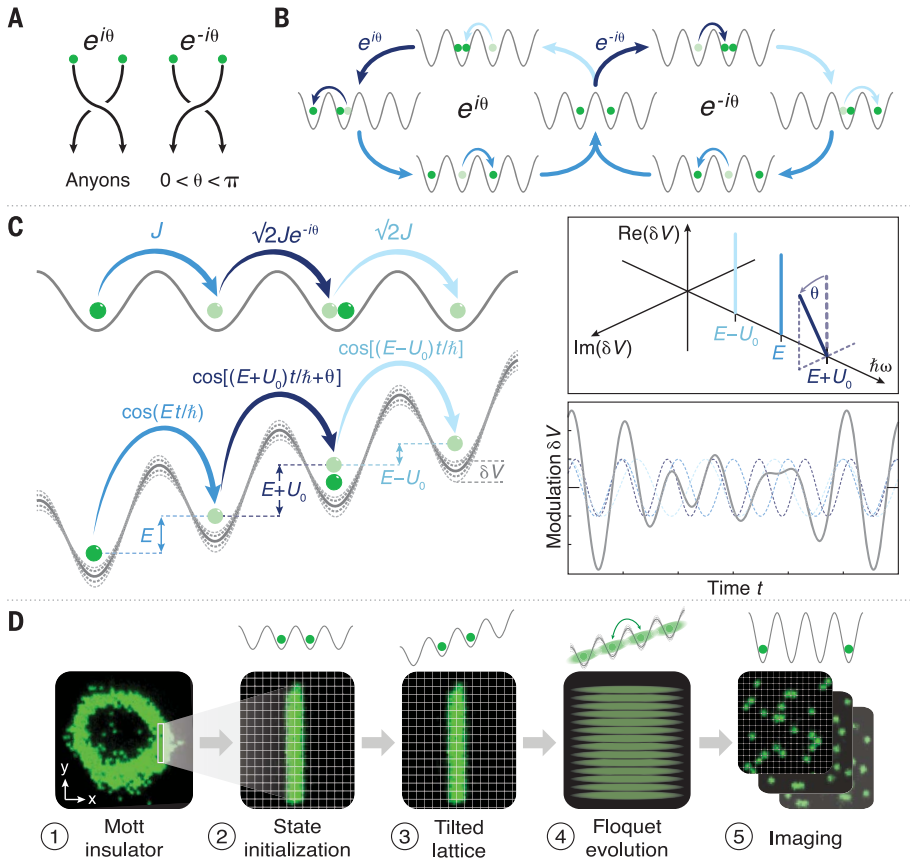

Fig. 1. Realization of anyons in one dimension. (**A**) In two dimensions, Abelian anyons have an exchange phase that interpolates between 0 (bosons) and π (fermions). (**B**) In one dimension, the wave function acquires phase −θ (or θ) when a particle tunnels right (or left) through an occupied site, analogous to clockwise (or counterclockwise) exchange in two dimensions. (**C**) We realize the AHM in a tilted optical lattice with energy offset E per site to suppress tunneling and then induce tunneling by modulating the lattice depth with three frequency (three-tone) components, each with amplitude δV: (i) E to tunnel from a singly occupied to an empty site, (ii) $E + U_0$ to tunnel from a singly occupied to a singly occupied site, and (iii) $E - U_0$ to tunnel from a doubly occupied to an empty site, where U_0 is on-site interaction in the initial Hamiltonian (*44*). Offsetting the phase of component $E + U_0$ by θ realizes the density-dependent Peierls phase. (Insets) Three-tone modulation in frequency (top) and time (bottom). The gray line is the sum of the three components (the dashed lines). (**D**) Experimental sequence: (1) and (2) Initialize two columns of atoms from a Mott insulator of ^{87}Rb. (3) Tilt the lattice and lower lattice depth V_x to prepare for modulation-induced tunneling. (4) Abruptly apply three-tone modulation to induce several independent quantum walks along x. (5) Project to the number basis and perform fluorescence imaging (*44*).

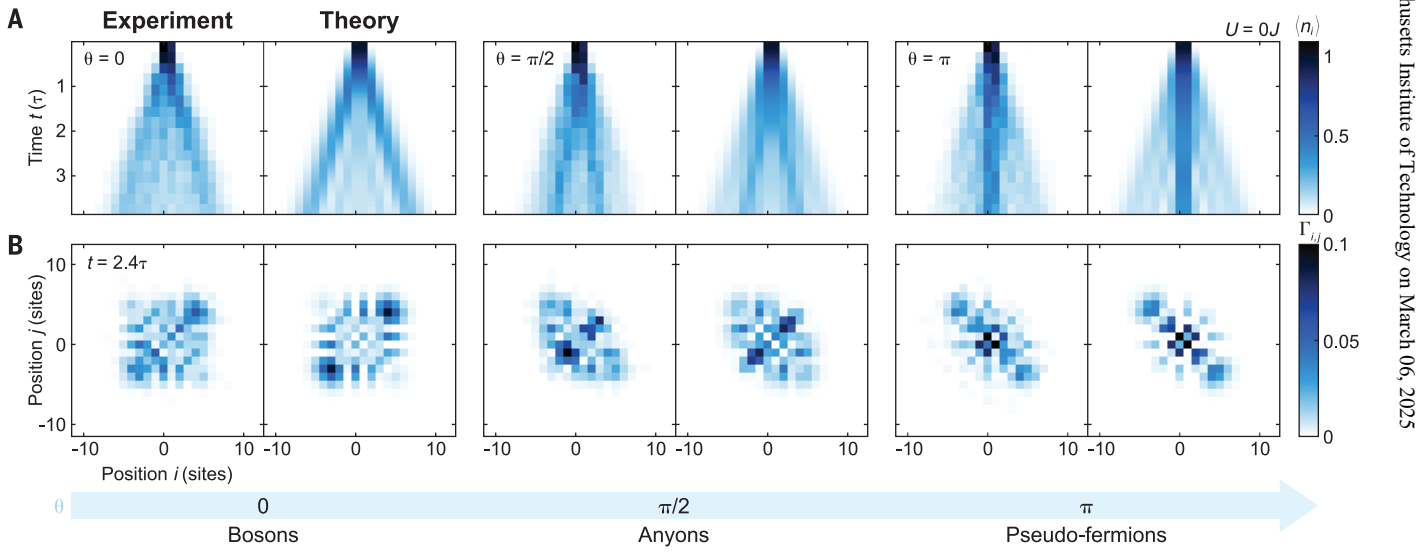

Fig. 2. Quantum walks of two anyons, $U = 0$. (**A**) Density profile of two-particle quantum walks for various θ, each obtained by averaging over the course of ~1800 experimental runs. Good agreement with theory shows coherence up to our experiment time $t \approx 4\tau$ (in units of inverse tunneling time $\tau = 15.0 \pm 0.3$ ms) across ~20 sites. (**B**) Density-density correlator Γ_{ij} at $t = 2.40 \pm 0.05\tau$. When $\theta = 0$, bosonic bunching appears as weights along the diagonal $i = j$. When $\theta = \pi$, antibunching behavior of pseudofermions appears as weights along the antidiagonal $i = -j$. When $\theta = \pi/2$, Γ_{ij} reveals fractional statistics, showing both strong diagonal weights and the onset of fermionization.

occupied site to an empty site, where U_0 is the interaction energy in the initial Hamiltonian (*44*). The amplitude of modulation δV determines J, and offsetting the phase of frequency component $E + U_0$ by θ from components E and $E - U_0$ realizes the density-dependent phase and therefore the statistical parameter. Modulating the lattice with these frequencies, which are resonant with parameters of the initial Hamiltonian, realizes the BHM with density-dependent phase corresponding to the noninteracting AHM. We can engineer an effective on-site interaction U in the AHM by detuning the sidebands to become $E - (U_0 - U)$ and $E + (U_0 - U)$ (*45*).

For the experiments that follow, we use the single-site control of our quantum gas microscope to study the dynamics of two anyons undergoing quantum walks, with and without interaction U in the AHM. Using a digital micromirror device (DMD) (*46*), we initialize two columns of atoms along y in a deep optical lattice of equal lattice depth $V_x = V_y = 45E_R$ along x and y, specified in units of the recoil energy $E_R = h \times 1.24$ kHz for our lattice constant of $a = 680$ nm, where h is the Planck constant, in preparation for several independent quantum walks of two particles along x (Fig. 1D). We ramp a magnetic field gradient to offset lattice sites by E and then lower V_x to $4E_R$ and abruptly turn on three-tone modulation with $\delta V = 20\% \times V_x$ to induce quantum walks along x. The parameters for the experiments are $J/h = 10.6 \pm 0.2$ Hz, $U_0/h = 210 \pm 4$ Hz, and $E/h = 800 \pm 3$ Hz, and we measure time in units of inverse tunneling rate $\tau = h/(2\pi J) = 15.0 \pm 0.3$ ms. We detect doubly occupied sites by ramping the magnetic field gradient past U_0 to separate atoms before imaging for half of each dataset, circumventing pairwise loss of atoms caused by light-assisted collisions (*44*).

Hanbury Brown–Twiss effect of 1D anyons

We first study anyonic behavior by measuring the quantum correlations of two particles simultaneously undergoing quantum walks when $U = 0$. The quantum walk of two particles is sensitive to quantum statistics owing to the Hanbury Brown–Twiss (HBT) effect, where all two-particle processes add coherently to develop quantum correlations (*34*, *39*, *47*–*49*). Initializing the state as $b_0^\dagger b_1^\dagger|0\rangle = |...0110...\rangle$, we capture the trajectory by evolving the system for successively longer periods of time before imaging and average over many images to obtain the probability distribution of the two particles (Fig. 2A). We capture the quantum walk trajectory for various θ and characterize quantum statistics using the density-density correlator $\Gamma_{i,j} = \langle b_j^\dagger b_i^\dagger b_i b_j \rangle$ (Fig. 2B). When θ = 0, bosonic bunching appears as weights along or near the diagonal $i = j$ of the correlation matrix $\Gamma_{i,j}$ (*39*), consistent with Bose-Einstein statistics. When θ = π, weights appear along or near the antidiagonal $i = -j$, indicating antibunching behavior emblematic of fermions. Weights appear along the diagonal $i = j$ because bosons now behave as pseudo-fermions, which do not obey the Pauli principle on-site, acting as fermions off-site and bosons on-site (*23*). Therefore, their spatial correlations differ from those of true fermions but nonetheless show the essential trait of antibunching. Finally, for fractional phase θ = π/2, the correlation matrix $\Gamma_{i,j}$ shows intermediate levels of bunching and antibunching to reveal fractional statistics; strong weights appear along the diagonal, whereas off-diagonal weights indicate the onset of fermionization. Good agreement with theory shows that the system maintains coherence up to our experiment time of $t \approx 4\tau$ across ~20 sites. Unless otherwise noted, all theoretical predictions were

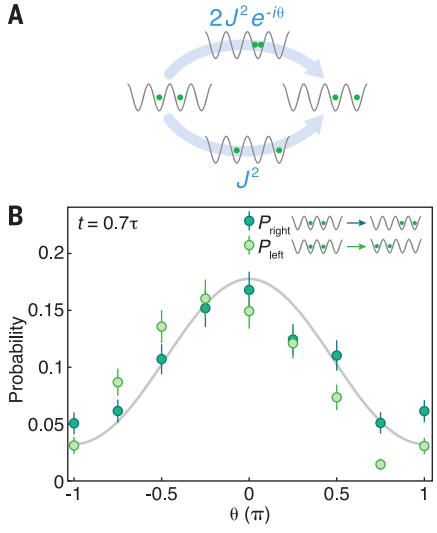

Fig. 3. Interferometric picture of Fock state evolution. (**A**) We can understand the effect of the statistical phase θ on tunneling processes by appealing to an interferometric interpretation of Fock state evolution. The initial state ($|...0110...\rangle$) splits into two arms, acquiring phase −θ in the upper arm ($|...0020...\rangle$) before interfering with the lower arm ($|...0101...\rangle$) to arrive at the final state ($|...0011...\rangle$). (**B**) Measured probability P_{right} of occupation of $|...0011...\rangle$, corresponding to both atoms having tunneled one site to the right after $t = 0.70 \pm 0.02\tau$ as a function of θ. The same relation holds for P_{left}, the probability for both atoms to tunnel one site to the left after $t = 0.70 \pm 0.02\tau$. Decrease in probability as θ approaches ±π can be understood as development of destructive interference between paths in Fock space, maximally cancelling when θ = ±π to localize atoms on their initial sites. The solid line shows prediction from theory (*44*). Error bars denote the SEMs.

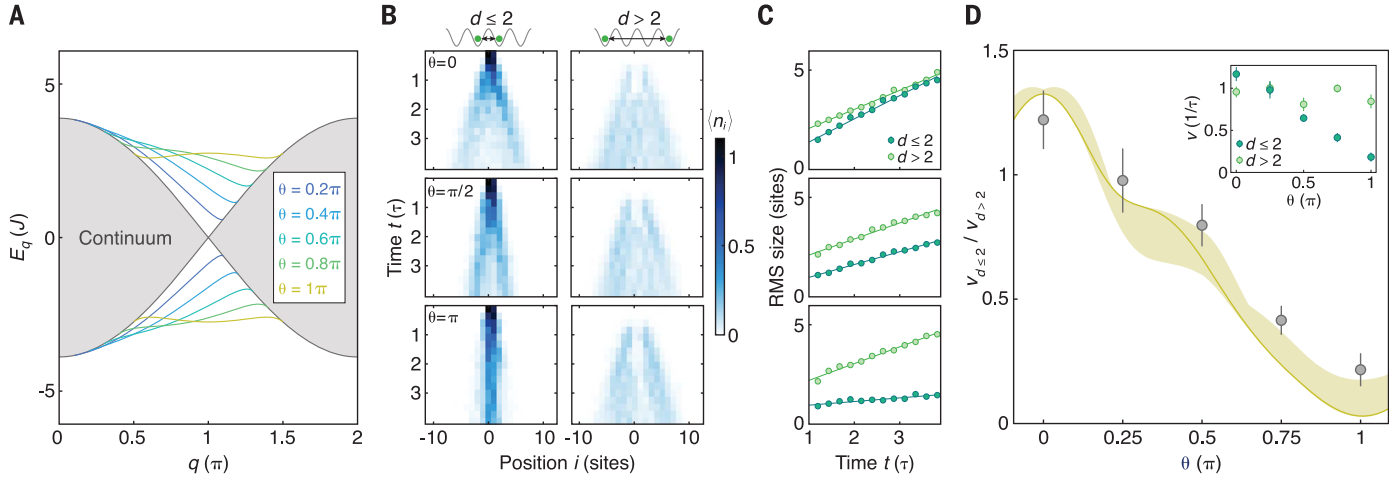

Fig. 4. Characterizing bound pairs of anyons, $U = 0$. (**A**) Two-particle spectrum E_q, where q is the center-of-mass quasimomentum, with scattering states forming a continuum (gray-shaded region) and bound states detaching from the continuum (solid lines; from blue to yellow: $\theta = m\pi/5$, $1 \leq m \leq 5$). (**B**) Density distributions conditioned on the relative distance d between the two particles undergoing a quantum walk (same data as in Fig. 2). Left (right) plots correspond to near (distant) particles separated by $d \leq 2$ ($d > 2$) sites, with θ = 0, π/2, and π, from top to bottom. (**C**) RMS size evolution of the near (dark green) and distant (light green) particle components, with θ = 0, π/2, and π, from top to bottom. The spreading velocities $v_{d\leq2}$ and $v_{d>2}$ are defined as the slopes of the linear fits (solid lines). Error bars (smaller than data points) were obtained from a bootstrap analysis. (**D**) Ratio of spreading velocities $v_{d\leq2}/v_{d>2}$ as a function of θ. The solid line shows theoretical prediction, with the shaded region corresponding to uncertainty in tilt calibration (*44*). (Inset) Spreading velocities $v_{d\leq2}$ and $v_{d>2}$ as a function of θ. Error bars denote the SEMs.

obtained ab initio using exact diagonalization of the BHM with density-dependent phase, with Hubbard parameters determined from the calibrated value of effective tunneling J (*44*).

A bimodal structure emerges in the density profiles, with an internal cone that narrows as θ increases from 0 to π amid a background density. We can understand this structure by appealing to an interferometric interpretation of Fock state evolution (Fig. 3A). Our initial state ($|...0110...\rangle$), the source, splits into upper ($|...0020...\rangle$) and lower ($|...0101...\rangle$) arms to interfere at the final state ($|...0011...\rangle$), a process that corresponds to both atoms tunneling one site to the right after a short time evolution $t < \tau$. When θ = 0, the two arms constructively interfere to arrive at the final state with enhanced probability, but when θ = π, the two arms destructively interfere, reducing the path to the final state, and the system is more likely to remain in the initial state. The same picture applies for tunneling leftward; hence, as θ increases from 0 to π, atoms are less likely to delocalize, forming the strong density pattern in the center in the pseudofermion limit. Notably, because the states composing the interferometer are the same as those in the loop in Fock space describing particle exchange (Fig. 1B), interference between the two arms directly reflects anyonic exchange statistics. We measure the Fock state distribution at short time $t = 0.70 \pm 0.02\tau$ and observe that the proportion P_{right} of experimental runs in state $|...0011...\rangle$ decreases as θ changes from 0 to ±π, as explained by the development of destructive interference in the interferometric picture of Fock state evolution (Fig. 3B). Because the same interferometric picture applies for tunneling leftward, the proportion P_{left} of experimental runs in $|...1100...\rangle$ at $t < \tau$ is approximately equal to P_{right}, also decreasing as θ changes from 0 to ±π thanks to destructive interference.

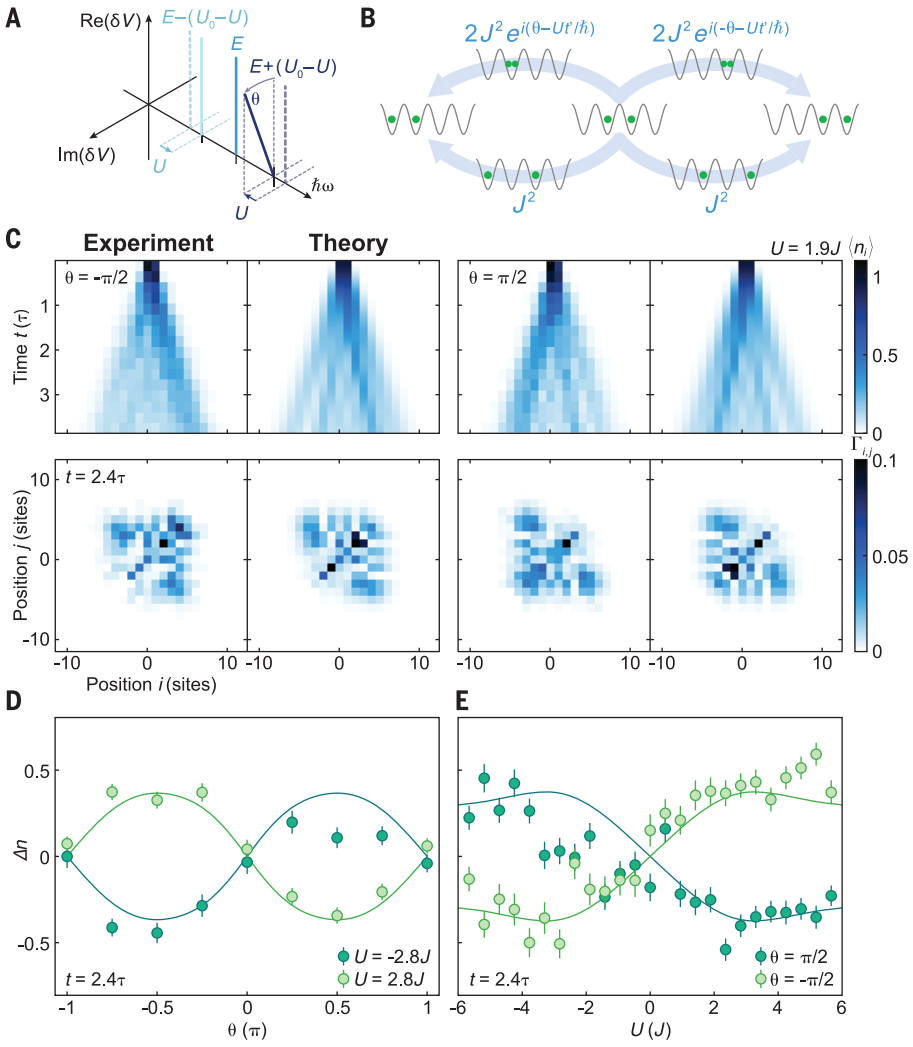

Fig. 5. Asymmetric transport owing to the presence of on-site interaction *U*. (**A**) Introducing repulsive on-site U in the AHM amounts to detuning sidebands $E - U_0$ and $E + U_0$ by U toward the center frequency E. (**B**) Presence of U breaks inversion symmetry in the density profiles of quantum walks for fractional θ. Now $P_{\text{right}} \neq P_{\text{left}}$ because the phase accumulated by tunneling right through an occupied site differs from that accumulated by tunneling left through an occupied site. (**C**) For $U = 1.9 \pm 0.4J$ and $\theta = -\pi/2$, the density profile shows a rightward trajectory and Γ_{ij} at $t = 2.40 \pm 0.05\tau$ shows strong spatial correlations with the right half of the quantum walk. Transport changes direction toward the left for $\theta = \pi/2$. (**D**) For constant $U = \pm 2.8 \pm 0.4J$, direction of transport as a function θ summarized by Δn, difference in atom number between right and left halves of the quantum walk. It changes with the sign of θ and with the sign of U, with $\Delta n \approx 0$ for $\theta = 0$ and π, consistent with symmetric expansion of bosons and pseudofermions. (**E**) For constant θ, direction of transport as a function of U. Direction of transport depends on the sign and the strength of U. Error bars denote the SEMs.

Bound states induced by the statistical phase

The narrowing internal cone in the density profiles indicates the formation of bound states as θ increases from 0 to π, even in the absence of on-site interaction U (*50*–*52*). This phenomenon occurs because the density-dependent gauge field mediates interactions between bosons (*31*, *45*, *53*). Theoretically, the two-particle spectrum of the AHM with $U = 0$ consists of a continuum of scattering states surrounded by two branches of bound states for $\theta \neq 0$—an upper branch with energy $E_q > 0$ and a lower branch with $E_q < 0$, where q is the center-of-mass quasimomentum (Fig. 4A). Each branch shows a preferred direction of propagation, given by the sign of the group velocity dE_q/dq. Our initial state $|...0110...\rangle$ projects onto both branches of bound states with equal weight and onto scattering states; therefore, the internal cone in the density profiles appears symmetric about the center (*44*).

We distinguish the formation of bound pairs from scattering states by analyzing the spreading velocities of the two wave function components. First, we characterize the two distinct dynamics by conditioning the density profiles in Fig. 2 on the relative distance d between the particles, separately analyzing the spatial distributions of near ($d \leq 2$ sites) and distant ($d > 2$ sites) particles (Fig. 4B); for analyses conditioned on different relative distances, which show similar behavior, see fig. S4 (*44*). Then, we determine the root mean square (RMS) size of each component as a function of time (Fig. 4C) and perform a linear fit to extract the spreading velocities $v_{d\leq 2}$ and $v_{d>2}$ (Fig. 4D, inset). We see that $v_{d>2}$ is approximately independent of θ, as expected for scattering states, whereas $v_{d\leq 2}$ strongly decreases as θ increases from 0 to π. This behavior is consistent with the narrowing internal cone in the density profiles and the decreasing group velocity dE_q/dq in the two-particle spectrum as θ increases

from 0 to π. Note that we systematically extract a slightly reduced velocity compared with theory owing to error in calibrating site offset E, which results in a residual tilt in the effective model (*44*). Therefore, we characterize the formation of bound pairs with the ratio $v_{d\leq 2}/v_{d>2}$, a quantity more robust to a residual tilt (Fig. 4D). Data points at $\theta = \pi/4$ and $\theta = 3\pi/4$ correspond to the analysis of density profiles of two-particle quantum walks subject to these phases (*44*). Good agreement with theory further demonstrates that our measurements show the existence of bound pairs in the absence of on-site interactions.

Breaking of inversion symmetry

A defining characteristic of 1D anyons is spatially asymmetric transport when interactions are present because the AHM is not inversion symmetric (*54*). Inversion symmetry is broken because phase $-\theta$ (or θ) is acquired when a particle tunnels to the right (or left) to an occupied site, a property that becomes apparent in the density profile of anyonic quantum walks when $U \neq 0$ (*54*). This can be understood by referring to the interferometric picture of Fock states at short time $t < \tau$ (Fig. 5B). Phases acquired in the upper arms $|...0200...\rangle$ and $|...0020...\rangle$ are now, respectively, $\theta - Ut'/\hbar$ and $-\theta - Ut'/\hbar$, where $t' = t/3$ (*44*), which for $\theta = 0$ or $\theta = \pi$, result in equal probability to arrive at final states $|...1100...\rangle$ and $|...0011...\rangle$. When θ is fractional, the probabilities to arrive at final states $|...1100...\rangle$ and $|...0011...\rangle$ are not equal, with preference to tunnel in a particular direction. This picture also explains that when the sign of θ or U changes, so does the direction of transport.

Introducing an effective on-site interaction in our scheme amounts to detuning the sidebands $E - U_0$ and $E + U_0$ by U (Fig. 5A), which, when present, leads to asymmetric transport in the density profile of two anyons undergoing quantum walks (Fig. 5C). The density profile shows transport toward the right when $\theta = -\pi/2$ and $U = 1.9 \pm 0.4J$, with $\Gamma_{i,j}$ at $t = 2.40 \pm 0.05\tau$ showing correlations with the right half of the quantum walk. For the opposite phase $\theta = \pi/2$, the direction of transport is now toward the left, corresponding to a reversal of phases accumulated in the left and right upper arms of the interferometer. We quantify the asymmetry of transport by the difference in atom number between the right and left halves of the quantum walk, $\Delta n = \sum_{i>0}\langle n_i\rangle - \sum_{i\leq 0}\langle n_i\rangle$, after some time evolution. At constant U, we see that transport is asymmetric for fractional θ and changes direction as θ reverses sign (Fig. 5D). When $\theta = 0$ or π, we measure $\Delta n \approx 0$, consistent with the symmetric density profiles of bosons and pseudofermions. At constant fractional θ, the direction of transport changes with the sign of U (Fig. 5E), behavior inherent only to anyons because expansion dynamics of bosons and fermions are identical for $\pm U$ (*55*–*57*). General agreement with theory shows that interactions can be engineered across a broad range, $-6J < U < 6J$, with deviations appearing when $U < 0$ owing to Floquet heating (*44*).

Discussion

We engineered a density-dependent Peierls phase to realize 1D anyons with tunable exchange phase and reveal fractional statistics in the HBT effect of two-anyon quantum walks. We show that this density-dependent phase, a form of interaction, is the mechanism behind the formation of bound states, even in the absence of on-site interactions. Then, once we introduce on-site interactions, the breaking of inversion symmetry—a property associated with fractional statistics—becomes apparent in the density profiles thanks to the interplay between the density-dependent phase and on-site interactions.

The three-tone Floquet scheme that realizes the AHM expands existing capabilities of Hamiltonian engineering, enabling control of U without Feshbach resonances and the simulation of a broad class of Hubbard models owing to the ability to independently control J, U, and θ. Floquet engineering with ultracold atoms is generally a challenge, requiring cancellation of coupling to dissipative modes (*58*) or an optimal balance between driving parameters and coherence time of the system (*59*). However, our postselection rate remains relatively high at ~60% at the end of a typical experiment lasting $t \approx 4\tau$, despite the number of modulation components (*44*). Additionally, numerical simulations suggest that heating rates remain low for systems of more than two particles that are of interest for future research (*45*). It would therefore be viable to expand the scheme, such as by increasing the number of modulation components or by dynamically changing effective Hubbard parameters, as well as the system size.

The many-body behavior of an ensemble of 1D anyons is a promising direction for future study. For example, the bound states that we observe play a crucial role in the emergence of the so-called partially paired phase, which consists of both paired and unpaired components (*30*, *31*). This phase, as well as other exotic phenomena (*23*, *28*), may be reached by adiabatically ramping Floquet parameters to connect to a target state. Our quantum gas microscope is also well suited for the microscopic study of entanglement properties of 1D anyons (*60*). Finally, ultracold atoms may offer a route to engineering non-Abelian anyons, such as those in the 1D wire construction for topological quantum computation (*61*), as suggested by similarities between the AHM and quasi-1D systems hosting non-Abelian anyons (*54*). Other directions include introducing three-body hard-core interactions (*20*, *24*) and controlling anyonic excitations in the Pfaffian state (*62*–*64*).

REFERENCES AND NOTES

1. J. M. Leinaas, J. Myrheim, *Nuovo Cim. B* **37**, 1–23 (1977).
2. F. Wilczek, *Phys. Rev. Lett.* **49**, 957–959 (1982).
3. M. Greiter, F. Wilczek, *Annu. Rev. Condens. Matter Phys.* **15**, 131–157 (2024).
4. B. I. Halperin, *Phys. Rev. Lett.* **52**, 1583–1586 (1984).
5. D. Arovas, J. R. Schrieffer, F. Wilczek, *Phys. Rev. Lett.* **53**, 722–723 (1984).
6. H. Bartolomei *et al*., *Science* **368**, 173–177 (2020).
7. J. Nakamura, S. Liang, G. C. Gardner, M. J. Manfra, *Nat. Phys.* **16**, 931–936 (2020).
8. R. Coldea, D. A. Tennant, A. M. Tsvelik, Z. Tylczynski, *Phys. Rev. Lett.* **86**, 1335–1338 (2001).
9. A. Kitaev, *Ann. Phys.* **321**, 2–111 (2006).
10. G. Semeghini *et al*., *Science* **374**, 1242–1247 (2021).
11. A. Kitaev, *Ann. Phys.* **303**, 2–30 (2003).
12. S. Bravyi, *Phys. Rev. A* **73**, 042313 (2006).
13. C. Nayak, S. H. Simon, A. Stern, M. Freedman, S. Das Sarma, *Rev. Mod. Phys.* **80**, 1083–1159 (2008).
14. D. J. Clarke, J. Alicea, K. Shtengel, *Nat. Commun.* **4**, 1348 (2013).
15. Google Quantum AI and Collaborators, *Nature* **618**, 264–269 (2023).
16. F. D. M. Haldane, *Phys. Rev. Lett.* **67**, 937–940 (1991).
17. M. Greiter, *Phys. Rev. B* **79**, 064409 (2009).
18. F. Wilczek, *Phys. Rev. Lett.* **48**, 1144–1146 (1982).
19. A. Kundu, *Phys. Rev. Lett.* **83**, 1275–1278 (1999).
20. N. Harshman, A. Knapp, *Ann. Phys.* **412**, 168003 (2020).
21. M. Bonkhoff *et al*., *Phys. Rev. Lett.* **126**, 163201 (2021).
22. G. Valentí-Rojas, A. J. Baker, A. Celi, P. Öhberg, *Phys. Rev. Res.* **5**, 023128 (2023).
23. T. Keilmann, S. Lanzmich, I. McCulloch, M. Roncaglia, *Nat. Commun.* **2**, 361 (2011).
24. S. Nagies, B. Wang, A. C. Knapp, A. Eckardt, N. L. Harshman, *SciPost Phys.* **16**, 086 (2024).
25. Y. Hao, Y. Zhang, S. Chen, *Phys. Rev. A* **78**, 023631 (2008).
26. Y. Hao, Y. Zhang, S. Chen, *Phys. Rev. A* **79**, 043633 (2009).
27. G. Tang, S. Eggert, A. Pelster, *New J. Phys.* **17**, 123016 (2015).
28. C. Sträter, S. C. L. Srivastava, A. Eckardt, *Phys. Rev. Lett.* **117**, 205303 (2016).
29. L. Yuan, M. Xiao, S. Xu, S. Fan, *Phys. Rev. A* **96**, 043864 (2017).
30. S. Greschner, L. Santos, *Phys. Rev. Lett.* **115**, 053002 (2015).
31. W. Zhang, S. Greschner, E. Fan, T. C. Scott, Y. Zhang, *Phys. Rev. A* **95**, 053614 (2017).
32. C. S. Chisholm *et al*., *Phys. Rev. Res.* **4**, 043088 (2022).
33. A. Frölian *et al*., *Nature* **608**, 293–297 (2022).
34. L. Sansoni *et al*., *Phys. Rev. Lett.* **108**, 010502 (2012).
35. J. C. F. Matthews *et al*., *Sci. Rep.* **3**, 1539 (2013).
36. W. Zhang *et al*., *Nat. Commun.* **13**, 2392 (2022).
37. W. S. Bakr, J. I. Gillen, A. Peng, S. Fölling, M. Greiner, *Nature* **462**, 74–77 (2009).
38. L. Wang, L. Wang, Y. Zhang, *Phys. Rev. A* **90**, 063618 (2014).
39. P. M. Preiss *et al*., *Science* **347**, 1229–1233 (2015).
40. L. W. Clark *et al*., *Phys. Rev. Lett.* **121**, 030402 (2018).
41. F. Görg *et al*., *Nat. Phys.* **15**, 1161–1167 (2019).
42. C. Schweizer *et al*., *Nat. Phys.* **15**, 1168–1173 (2019).
43. F. Wilczek, *Fractional Statistics and Anyon Superconductivity* (World Scientific, 1990).
44. Materials and methods are available as supplementary materials.
45. L. Cardarelli, S. Greschner, L. Santos, *Phys. Rev. A* **94**, 023615 (2016).
46. P. Zupancic *et al*., *Opt. Express* **24**, 13881–13893 (2016).
47. M. Henny *et al*., *Science* **284**, 296–298 (1999).
48. T. Jeltes *et al*., *Nature* **445**, 402–405 (2007).
49. A. Peruzzo *et al*., *Science* **329**, 1500–1503 (2010).
50. K. Winkler *et al*., *Nature* **441**, 853–856 (2006).
51. T. Fukuhara *et al*., *Nature* **502**, 76–79 (2013).
52. F. Kranzl *et al*., *Phys. Rev. X* **13**, 031017 (2023).
53. S. Greschner, L. Cardarelli, L. Santos, *Phys. Rev. A* **97**, 053605 (2018).
54. F. Liu, J. R. Garrison, D.-L. Deng, Z.-X. Gong, A. V. Gorshkov, *Phys. Rev. Lett.* **121**, 250404 (2018).
55. U. Schneider *et al*., *Nat. Phys.* **8**, 213–218 (2012).
56. J. P. Ronzheimer *et al*., *Phys. Rev. Lett.* **110**, 205301 (2013).
57. J. Yu, N. Sun, H. Zhai, *Phys. Rev. Lett.* **119**, 225302 (2017).
58. K. Viebahn *et al*., *Phys. Rev. X* **11**, 011057 (2021).
59. A. Eckardt, *Rev. Mod. Phys.* **89**, 011004 (2017).

60. R. Islam *et al*., *Nature* **528**, 77–83 (2015).
61. J. Alicea, Y. Oreg, G. Refael, F. von Oppen, M. P. A. Fisher, *Nat. Phys.* **7**, 412–417 (2011).
62. A. Sterdyniak, N. Regnault, G. Möller, *Phys. Rev. B* **86**, 165314 (2012).
63. F. A. Palm *et al*., *Phys. Rev. B* **103**, L161101 (2021).
64. J. Léonard *et al*., *Nature* **619**, 495–499 (2023).
65. J. Kwan *et al*., Realization of 1D anyons with arbitrary statistical phase, V1, Harvard Dataverse (2024); https://doi.org/10.7910/DVN/HF5ONJ.

ACKNOWLEDGMENTS

We thank M. Lebrat, J. Léonard, M. E. Tai, T. Esslinger, N. Harshman, F. Liu, S. Nagies, H. Pichler, L. Santos, and B. Wang for valuable discussions. **Funding:** We acknowledge support by the ONR (award no. N00014-18-1-2863), LBNL/DoE QSA (award no. DE-AC02-05CH11231), ARO (award no. W911NF-20-1-0021), the Gordon and Betty Moore Foundation (award no. GBMF-11521), and NSF (award nos. PHY-1734011, PHY-2317134, and OAC-2118310). A.E. was supported by the Deutsche Forschungsgemeinschaft (DFG) through the Research Unit FOR 2414 under project no. 277974659. A.V.G. was supported in part by the NSF QLCI (award no. OMA-2120757), AFOSR, DoE ASCR Accelerated Research in Quantum Computing program (award nos. DE-SC0020312 and DE-SC0025341), DoE ASCR Quantum Testbed Pathfinder program (award nos. DE-SC0019040 and DE-SC0024220), NSF STAQ program, ARO MURI, AFOSR MURI, and DARPA SAVaNT ADVENT. Support is also acknowledged from the US Department of Energy, Office of Science, National Quantum Information Science Research Centers, Quantum Systems Accelerator. A.V.G. is required to disclose that he is also an Amazon Scholar at Amazon Web Services. **Author contributions:** J.K., P.S., Y.L., B.B.-H., and M.G. conceptualized the experiment. J.K., P.S., Y.L., S.K., and B.B.-H. collected and analyzed data. J.K. and B.B.-H. performed numerical simulations. J.K., B.B.-H., A.V.G., and A.E. performed theoretical analysis. M.G. supervised the work. J.K., P.S., Y.L., A.V.G., A.E., B.B.-H., and M.G. wrote the manuscript. **Competing interests:** M.G. is a cofounder and shareholder of QuEra Computing. All other authors declare no competing interests. **Data and materials availability:** Experimental data and analysis code are available on Harvard Dataverse (*65*).

SUPPLEMENTARY MATERIALS

science.org/doi/10.1126/science.adi3252
Materials and Methods
Supplementary Text
Figs. S1 to S7
References (*66*–*73*)

Submitted 18 April 2023; accepted 25 October 2024
10.1126/science.adi3252